Active flow control inside the S-duct using AC-DBD plasma actuators

Fan Jiang[1], Konstantinos Kontis [2], Craig White[3]
School of Engineering, James Watt South Building, Glasgow, G12 8QQ
[1]: 2288394j@student.gla.ac.uk
[2]: kostas.kontis@glasgow.ac.uk
[3]: craig.white.2@glasgow.ac.uk

Abstract

The S-duct has been widely studied in the aviation field. Improving the total pressure recovery coefficient by flow control method has always been a research hotpot (mainly to improve the flow separation in the S-duct). The AC-DBD flow control method has also been widely studied in recent decades. Researchers have carried out many experiments on DBD plasma actuators in a quasi-static environment. Limited by the small magnitude of the plasma-induced velocity (<10m/s), there is still little experimental data in the large Reynolds number scenario. This paper aims to study the application of AC-DBD plasma inside the S-duct (R_e>100k).

1.Introduction:

The diffusing S-duct is widely used in flight propulsion systems to connect the fuselage to the engine compressor. Due to the large duct curvature, flow separation is inevitable in the S-duct. Flow separation plus the effect of the secondary flow will result in the total pressure reduction and exacerbating flow distortion in the AIP interface (AIP: aerodynamic intake plane) [10,11]. A well-designed S-duct can efficiently reduce the flow separation, thus lowering total pressure loss [5]. Additionally, a well-designed S-duct can make the air in front of the engine more uniform, which usually means the engine can perform better [13-16]. In this paper, the experiment adopts a 3D printing S-duct, which has the same geometry as Welborn's experiment. The adopted flow control method is AC-DBD plasma flow control (AC-powered DBD plasma actuator).

DBD plasma flow control is an active flow control method. The principle is shown in Fig.1. A fundamental DBD plasma actuator contains an anode, a cathode, and a dielectric barrier to separate the anode and the cathode [8, 17]. An anode can discharge on one side (asymmetric DBD plasma) and both sides (symmetric DBD plasma). Fig.2 shows these two configurations. It does not need extra moving parts and has the advantages of low weight, fast response speed, and a slight influence on aerodynamic shape [12, 17]. Due to the advantages mentioned above, many scholars have studied it; however, so far, the research on its operation mechanism is still in a relatively immature stage. Due to the self-limiting characteristics of AC-DBD, the highest recorded induced velocity is only 10m/s [9].
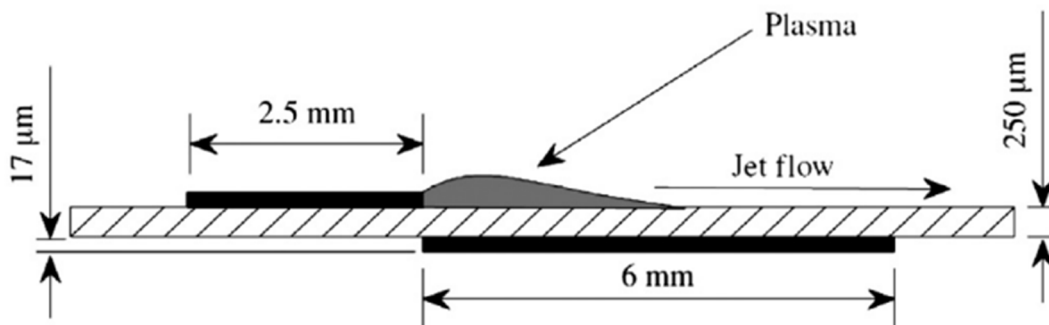
Fig.1. Asymmetric DBD plasma actuator principal schematic [1].
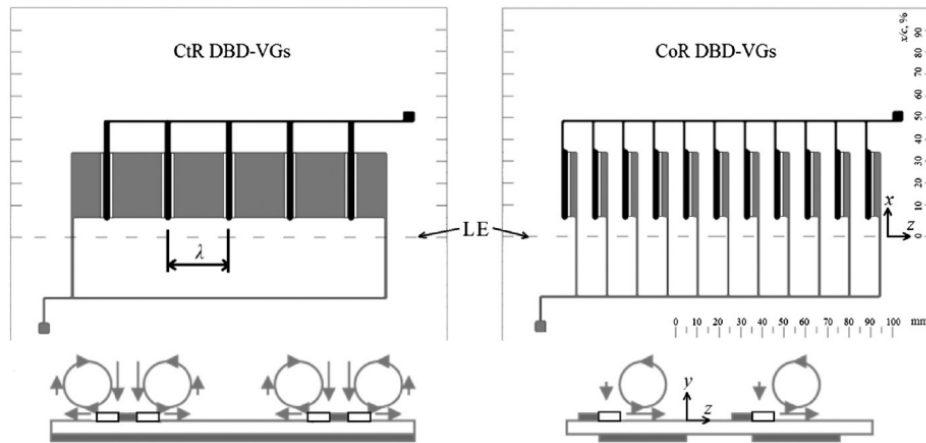
Fig.2. Symmetric (left) and asymmetric (right) DBD plasma actuators [2].

According to the working principle, the plasma actuator can be divided into wall jet and vortex generators. The wall jet is shown in Fig.1. The wall jet induced by the DBD plasma does not add extra mass to the flow. According to the study by Jukes and Choi (2012), the operation mechanism of the plasma-wall jet is that the fluid above and upstream of the DBD plasma actuator is induced to move towards the DBD plasma actuator and then being accelerated laterally to form the laminar wall jet [3]. Fig.3 shows the time-averaged velocity field of the plasma-wall jet.
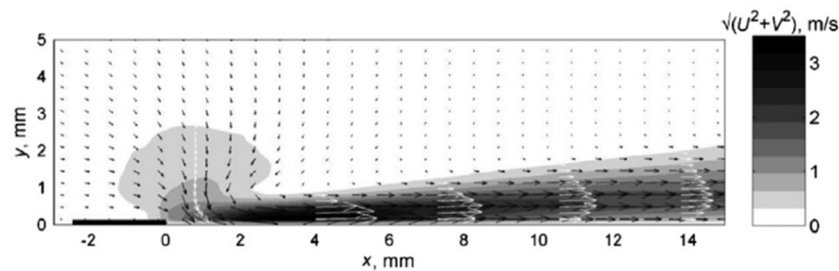
Fig.3. Time-averaged velocity field induced by a single asymmetric DBD plasma actuator in quiescent air [3].

Vortex generator configuration uses the principle of starting vortex generated when DBD plasma actuators initiate. This phenomenon was first discovered by Post (2004) [4]. This starting vortex introduces momentum from the main flow to the boundary layer. The principle is similar to the vortex generators. Fig.2 shows co-rotating and counter-rotating plasma vortex generator arrays.

This paper aims to study the application of the AC-DBD plasma flow control technique inside the S-duct. Also, the performance of various configurations of plasma actuators is investigated and compared. Moreover, this paper explores the feasibility of applying AC-DBD plasma actuators in large Reynolds number scenarios(>100k). The experiment data is acquired by the 7-hole probe and analyzed along with plot and data analysis software Tecplot.

2. Experiment Setup

The experiment schematic is shown in Fig.4. The whole experiment system consists of S-duct, traverse system, transparent acrylic box and a fan. The traverse system is housed in the acrylic box, and the box connects the S-duct to the fan.
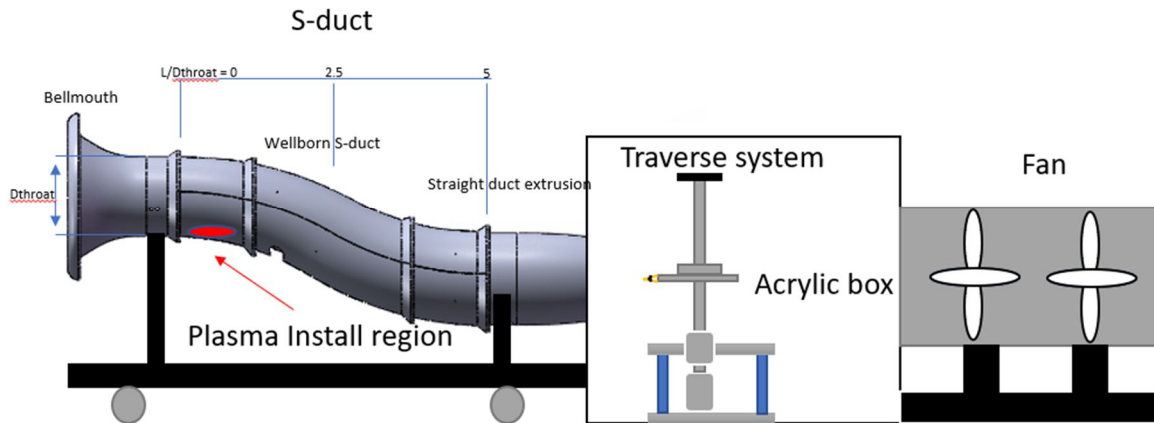
S-duct

Fig.4. The experiment schematic.

2.1 Experiment Facility

The diffusing S-duct geometry uses Wellborn's design [5]. Fig.5 is the schematic of the Wellborn's S-duct design. Two planar arcs define the S-duct centerline, the arc radius is 102.1cm and the arc subtended angle is 30°. The inlet radius is 10.21cm (r1), and the outlet radius is 12.57cm (r2). The radius elsewhere follows equation 1.

$$\frac{r}{r_1} = 1 + 3\left(\frac{r_2}{r_1} - 1\right)\left(\frac{\theta}{\theta_{max}}\right)^2 - 2\left(\frac{r_2}{r_1} - 1\right)\left(\frac{\theta}{\theta_{max}}\right)^3 \qquad eq.1$$
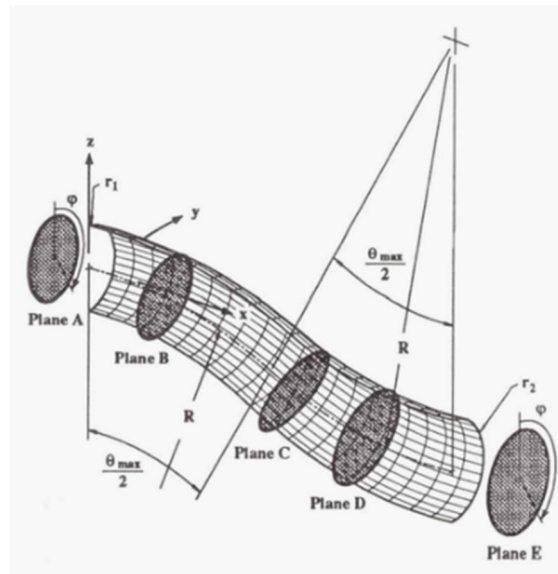
Fig.5. Half shell of the circular diffusing S-duct [5].

As shown in Fig. 4, the inlet diameter of the S-duct in the experiment is 435 mm (Dinlet), the throat diameter (Dthroat) is 204.2 mm, and the outlet diameter (DAIP) is 251.4mm, the length of bell mouth and duct extrusion are both 350 mm. This S-duct is manufactured by 3D printing, and the material is nylon plastic.

The interior space of the acrylic box is a cube with a side length of 1 meter. The traverse system housed in the box contains two stepper motors. The technical specifications are
- 400 steps per millimetre in the horizontal direction,
- 25 millimetres per second,
- corresponding to a screw stroke of 64 cm, and
- 410 steps per millimetre in the vertical direction.

The stepper motor brand is Schrittmotormodul, the type is MS200HT2, I = 3.0 A, M23 12pol. The pressure

measurement system mainly contains a 7-hole probe and ZOC pressure scanner. The 7-hole probe, at the first beginning, was applied in the joint research between NASA-Ames and U.S. Air Force Academy and is also the product of that joint research [6]. It can handle more complex flow conditions (maximum can be able to measure the incoming flow parameters at 75° to the probe's central axis). The ZOC pressure scanner system is connected to the 7-hole probe and is used to collect and process data from the 7-hole probe. This system contains four modules; each module has eight channels. The sample collection time (period) is set to 50. The unit is microseconds. The number of data collection frames is 50, namely, collecting data 50 times at this position. The sample average is set to 50. These parameters mean that 50 sets of data will be collected in 50 microseconds and then divided by 50; the average is the last recorded data. A MATLAB program is used to run this system.

The fan is EQ511467, manufactured by Flakt Woods. The fan diameter is 500 millimetres, the blade number is 5, and the maximum fan speed is 1380 rpm (12.3 m/s). A 220V-240V power supply powers it. The power is divided into ten levels, ten is the largest, and one is the smallest. In this experiment, the fan was operated with relatively lower power.

2.2 Plasma Actuator Setup

The whole plasma system consists of a power supply, voltage amplifier, and plasma actuator (as shown in Fig.6).
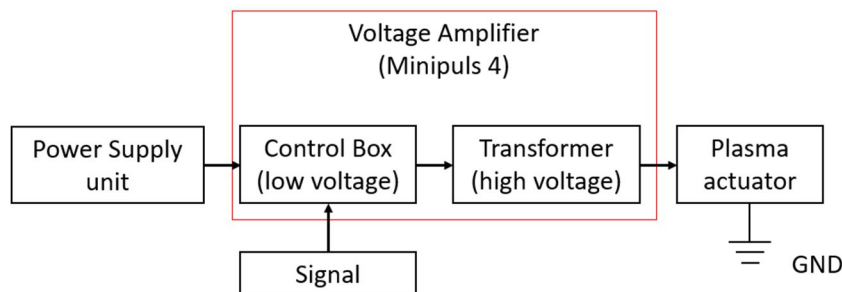
Fig.6. The schematic of the plasma system

The power supply is VSP2410 from the Voltcraft Company. It is a variable DC power supply. It can be able to provide a stable 30V-voltage during the experiment. The voltage amplifier is Minipuls4 manufactured by GBS Elektronik. According to the manual of Minipuls 4, the Minipuls 4 kit consists of two parts (as shown in Fig.7). one is an entire bridge board, which is all low voltage and can receive external signals. The other is a cascaded board of high voltage conversion. This kit is connected to a computer and controlled by a LabVIEW program.
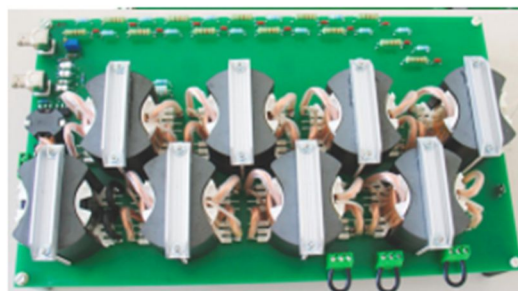
Fig.7. The Minipuls 4 Schematic

In this experiment, according to the configuration, the plasma actuators are divided into two categories, one is

symmetrical, and the other is asymmetrical. As shown below:
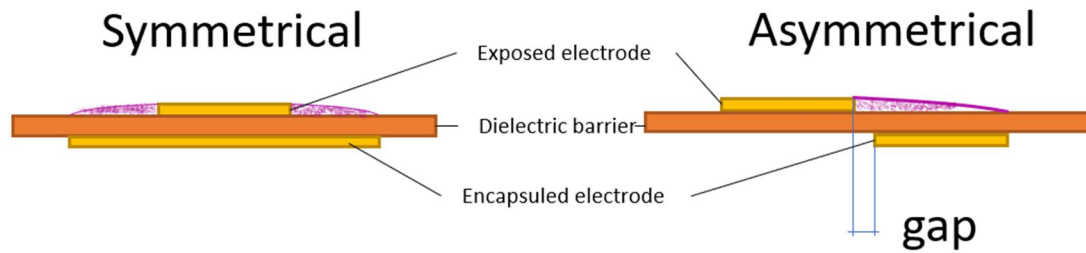
Fig.8. The plasma actuators configurations schematic

Symmetrical plasma actuators can be used as vortex generators, and asymmetrical plasma actuators can be used as wall jets. The materials for cathode and anode are copper foil. The thickness of the copper foil is 0.1mm. For these two types, the dielectric barrier materials are Kapton tapes. The thickness of a single layer of Kapton tape is 0.1mm. 4 layers of Kapton tapes are used in the experiment, which means the thickness of the dielectric barrier is 0.4mm. The experiment runs for a long time, and the data collection time is over 1 hour. The excitation voltage is 17kv. After the experiment test, when the thickness of the dielectric barrier is smaller than 0.4mm, the dielectric barrier cannot keep from being broken down for a long time.

Three plasma actuator configurations are used in the experiment. They are shown in Fig.9. For configuration ① (symmetrical type), the width of a single anode is 3mm, and the length of the overlap between the cathode and anode is 25mm. There are a total of 7 anodes in configuration ①. As for configuration ② and ③ (asymmetrical type), the geometries are the same. The anode width is 5mm, and the cathode width is 10mm. The overlap length is 70mm. Each configuration contains multiple plasma actuators, that is because the influence of a single plasma actuator is minimal. All configurations are symmetrically mounted. Configuration① is in the region of L/D 0.115 – 0.172. Configuration ② is in the region of L/D 0.115 – 0.31. Configuration ③ is in the region of L/D 0.115 – 0.47.
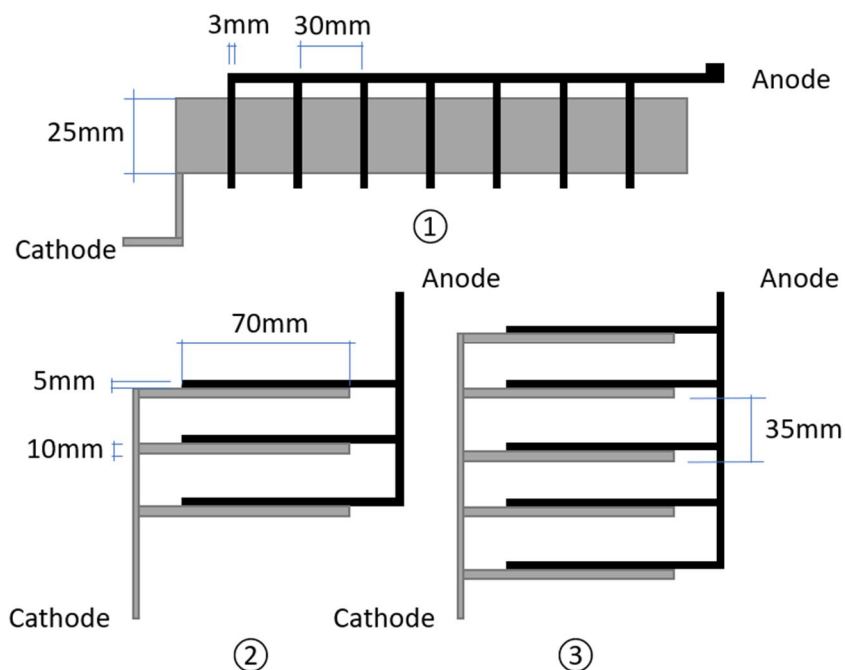
Fig.9. The schematic of plasma configurations (①: symmetrical type (vortex generator); ②③: asymmetrical type (wall jets))

For configurations ② and ③, excitation voltage is 17kv; frequency is 4khz, the voltage waveform is a square wave, 50% positive value and 50% negative value, as well as steady excitation. As for configuration ①, there are five excitation modes; the voltage and frequency are still 17kv and 4khz. According to different duty cycles, there are four modes when the modulation frequency is 400. The duty cycles respectively are 10, 20, 30 and 40. For example, when the modulation frequency is 400, the duty cycle is 10, meaning dividing a second into 400 cycles and only the first 10 per cent of each cycle is active. The fifth mode has a duty cycle of 50 and a modulation frequency of 1. The modulation frequency selects 400, which references the air velocity of 20m/s, and the length of the VG anode is 25mm. If the vortex can appear every time the excitation is activated, the vortex generated before and after will not interfere with each other, and the vortices will be relatively continuous. The modulation frequency selects 1, and the duty cycle is 50, ensuring that the starting vortex can appear [1].

3. Results and discussions

The fan's power is level 1; namely, it runs at the minimum power. Meanwhile, at the throat of the S-duct, the average difference between the static pressure measured at the top and the ambient barometric pressure is -170 Pa, and at the bottom is -230 Pa. The air density currently is about 1.199 kg/m3. According to equations (1) and (2), it can be known that the velocity at the top of the throat is about 16.85m/s, and the velocity at the bottom is about 19.57m/s.

$$P_{total} = P_{static} + P_{dynamic} \qquad eq.\,(1)$$

$$P_{dynamic} = \frac{1}{2} \cdot \rho_{air} \cdot v^2 \qquad eq.\,(2)$$

The data collection points take the centre of the AIP interface as the centre of the circle, 12 equally spaced concentric circles with a spacing of 9.8mm, and 10 points are evenly distributed on each circle, as shown in Fig. 10. The circle centre is measured once at the beginning, and the probe returns to the centre at the end to measure again. Therefore, a total of 122 points will be measured. The distance between the top of the probe and the AIP interface is about 5cm. The pressures measured by the probe are relative (relative to ambient pressure).
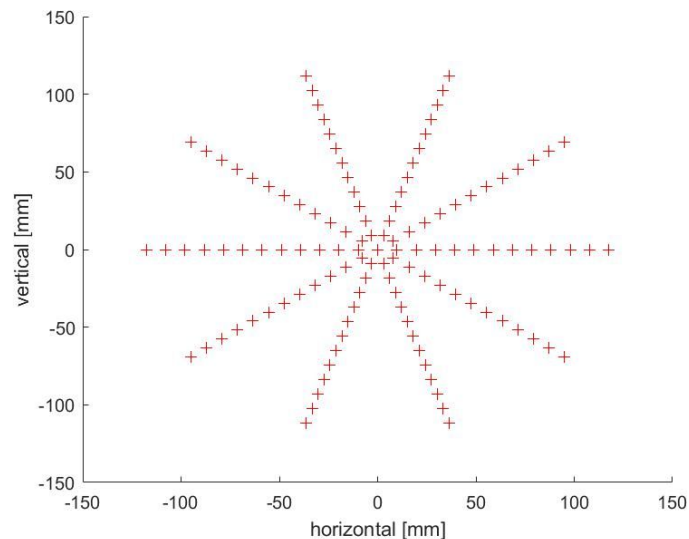
Fig. 10. The positions of data collection points

3.1 AIP interface characteristics (without plasma)

Figs. 11-15 show the physical characteristics of the AIP interface. (a), (b), (c), and (d) are all baseline data. (a) and (b) were measured on the same day. (c) and (d) were measured on the same day. It can be known from Figs. 11-15 that those distributions of various data are similar on the same day. Especially for U, V, and W, their values are extremely close. As for the stagnation pressure, when measuring (a) and (b), the barometric pressure at the beginning of the experiment was 98065Pa, the ambient temperature was 11.9℃, and the air density was about 1.199kg/m3. For (a) and (b), the stagnation pressure averages of 122 measurement points are respectively -

30.24Pa and -30.03Pa, with an error of only 0.6%. When measuring (c) and (d), the ambient pressure and temperature were 97457Pa and 11.6℃, and the air density was about 1.1903kg/m3. The stagnation pressure averages of (c) and (d) are respectively -25.13 and -28.25, with an error of about 10%. The error between (c) and (d) is significant because the temperature and pressure vary greatly during that day. For (c) and (d), at the end of the experiment, the ambient pressure was 103113Pa, the temperature was 15.6℃, and the air density was about 1.2449kg/m3. Results measured on different days vary widely. To eliminate the environment's influence on the experiment as much as possible, the two groups of experiments for comparison will not only be carried out on the same day but also repeated several times for verification.

Fig. 11 shows the stagnation pressure distributions on the AIP interface. It can be seen from the figure that there a low-pressure area at the top and the bottom of the AIP interface. The region of low pressure at the top is more pronounced because the region where the flow separation occurs at the top is closer to the outlet interface (as shown in Fig. 16), and there is not enough distance for the main flow to reattach the wall. Corresponding to the flow at the bottom, the flow separation has also occurred. However, it is far from the outlet, and the main flow has begun to reattach the wall. There are two low-pressure cores in the flow separation region at the top; combined with the W velocity component distributions, there should be something like two oppositely rotating vortices in the flow separation region.
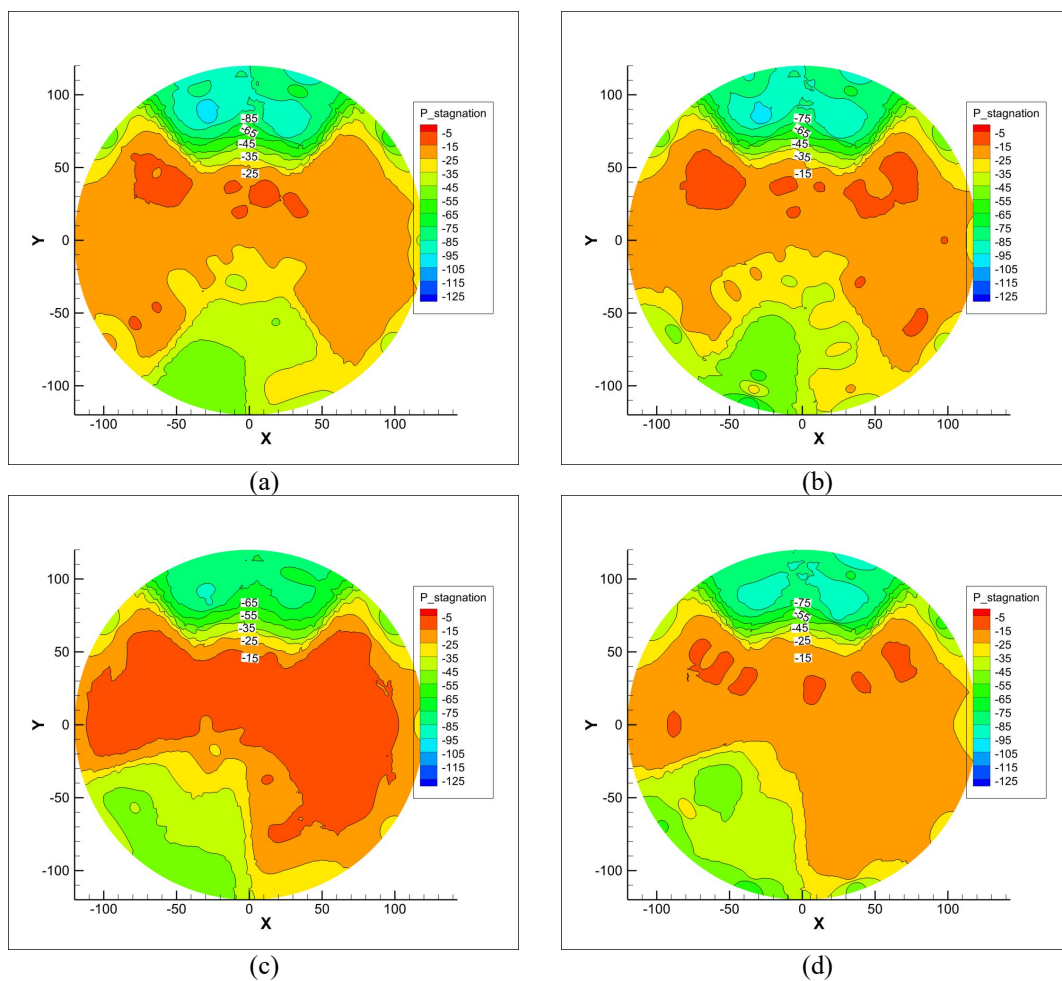
Fig. 11. Stagnation pressure distribution on the AIP interface

In the Fig. 12, as can be seen from the streamline, the main flow has a slight downward flow trend. Combined U and V velocity components, compared with the U velocity component, the magnitudes of V and W are very small. V is only 3% to 4% of U, and W is only about 1% of U. Detailed UVW average values are listed in Table 1.
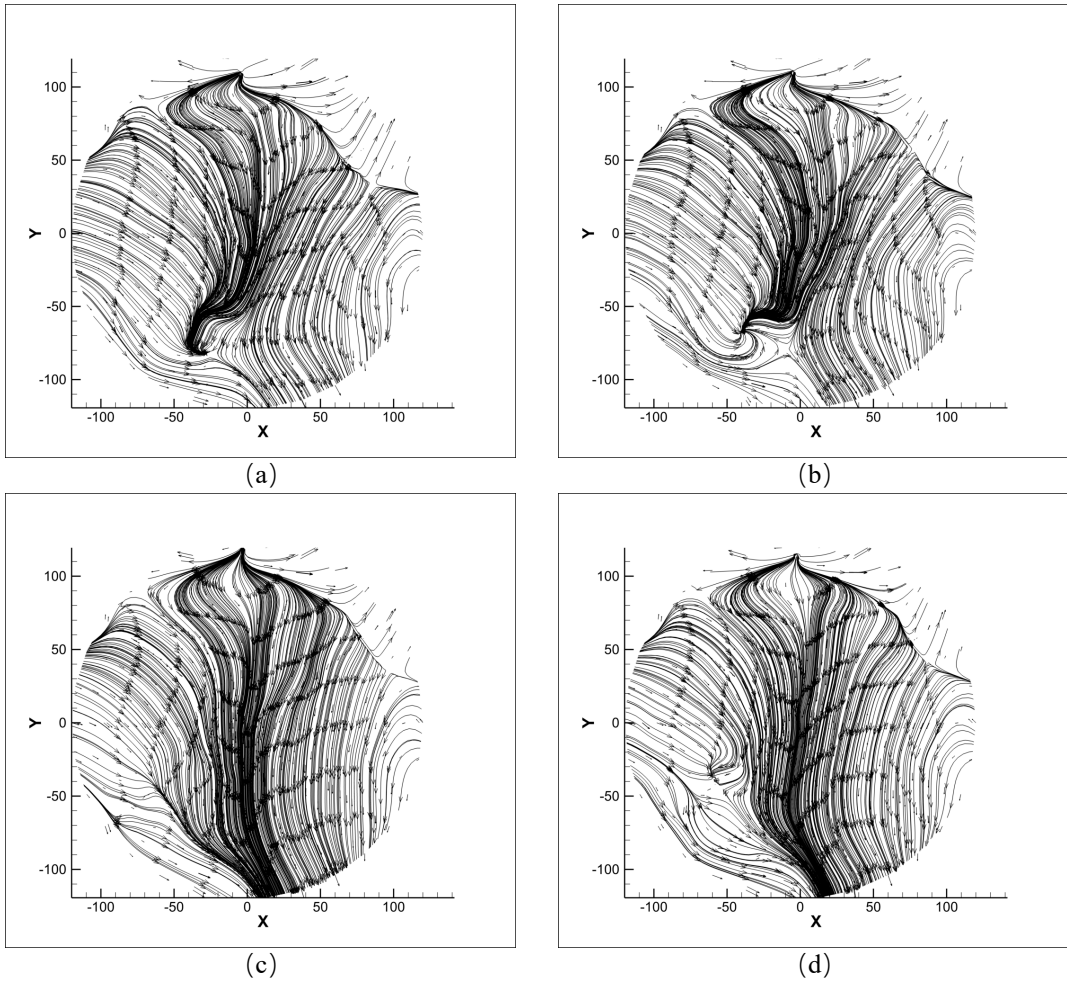
Fig. 12. The streamlines on the AIP interface

(c)

(d)
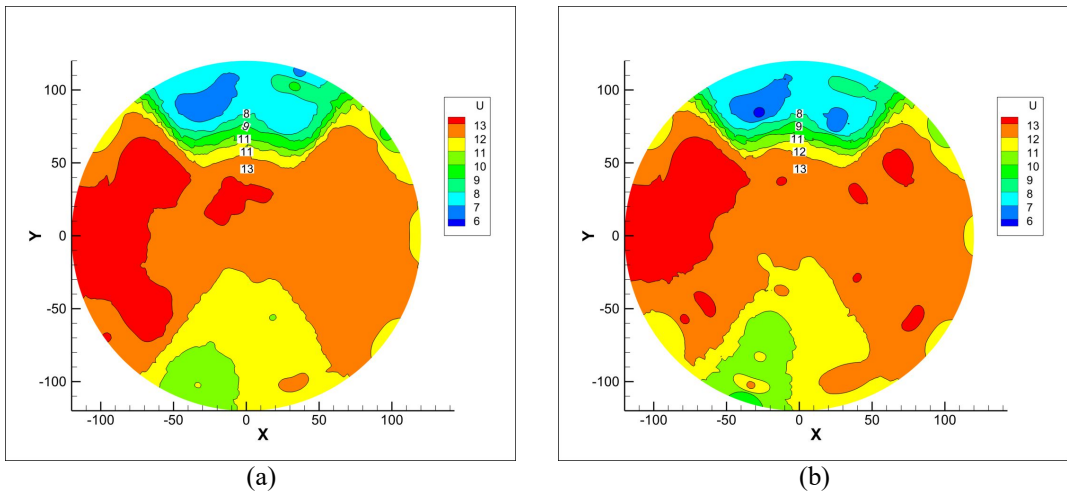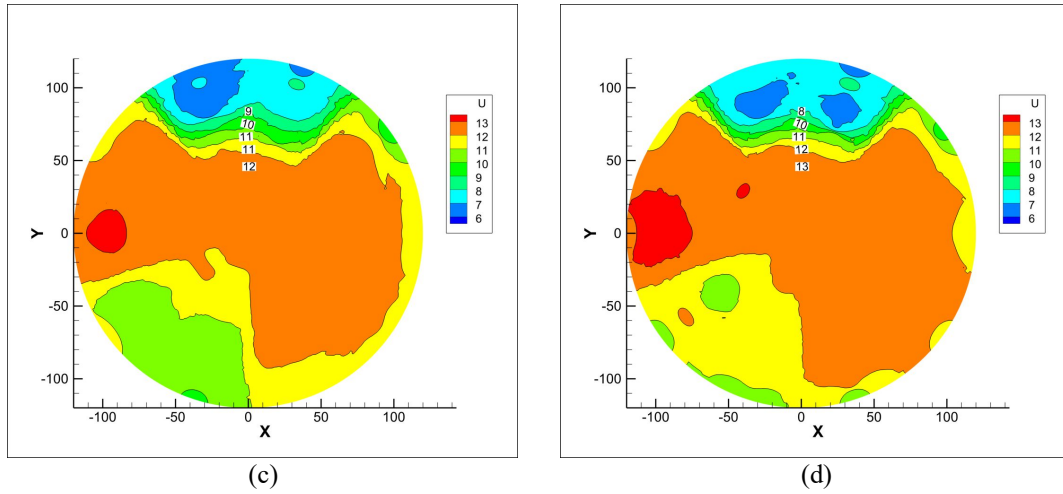
Fig. 13. The distribution of velocity components perpendicular to the AIP interface (U)

(a)

(b)

(c)

(d)
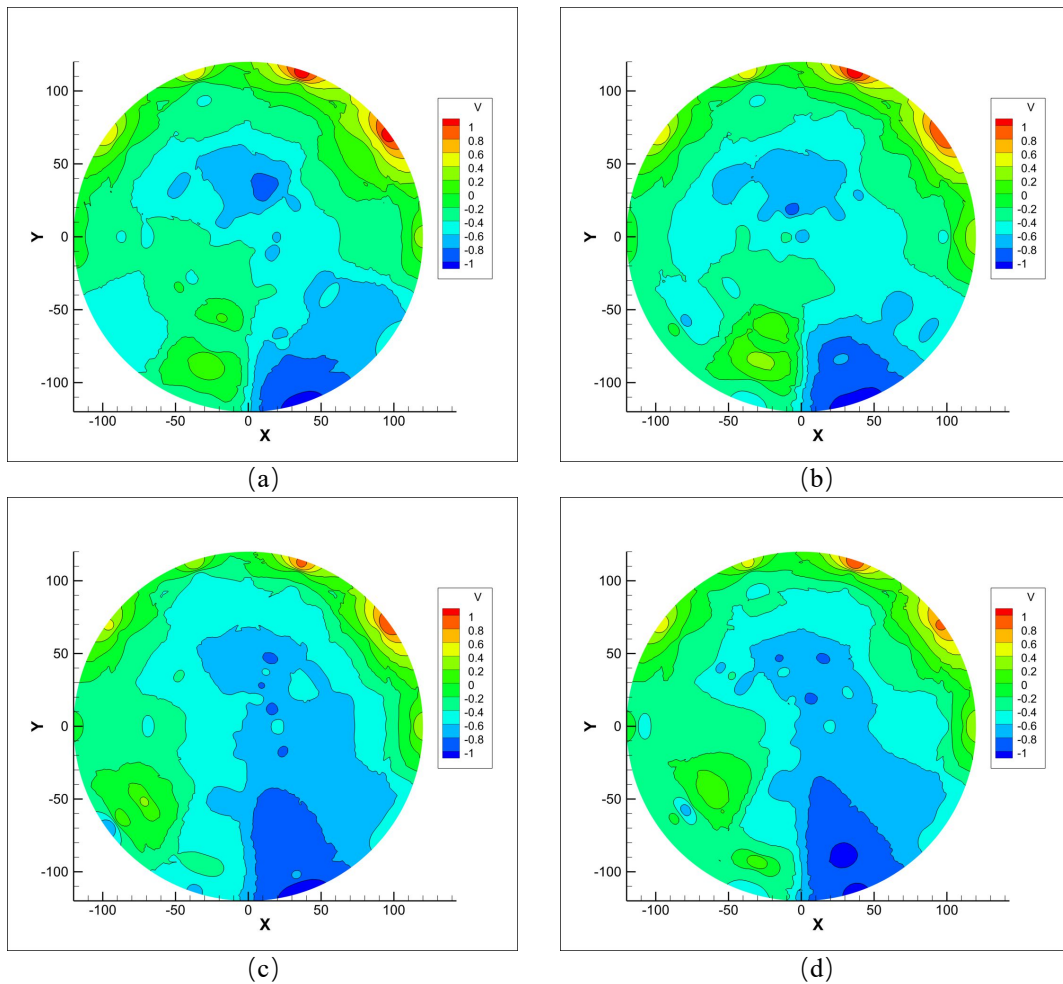
Fig.14. The distribution of velocity components in the Y direction on the AIP interface (V)

(a)

(b)

(c)

(d)
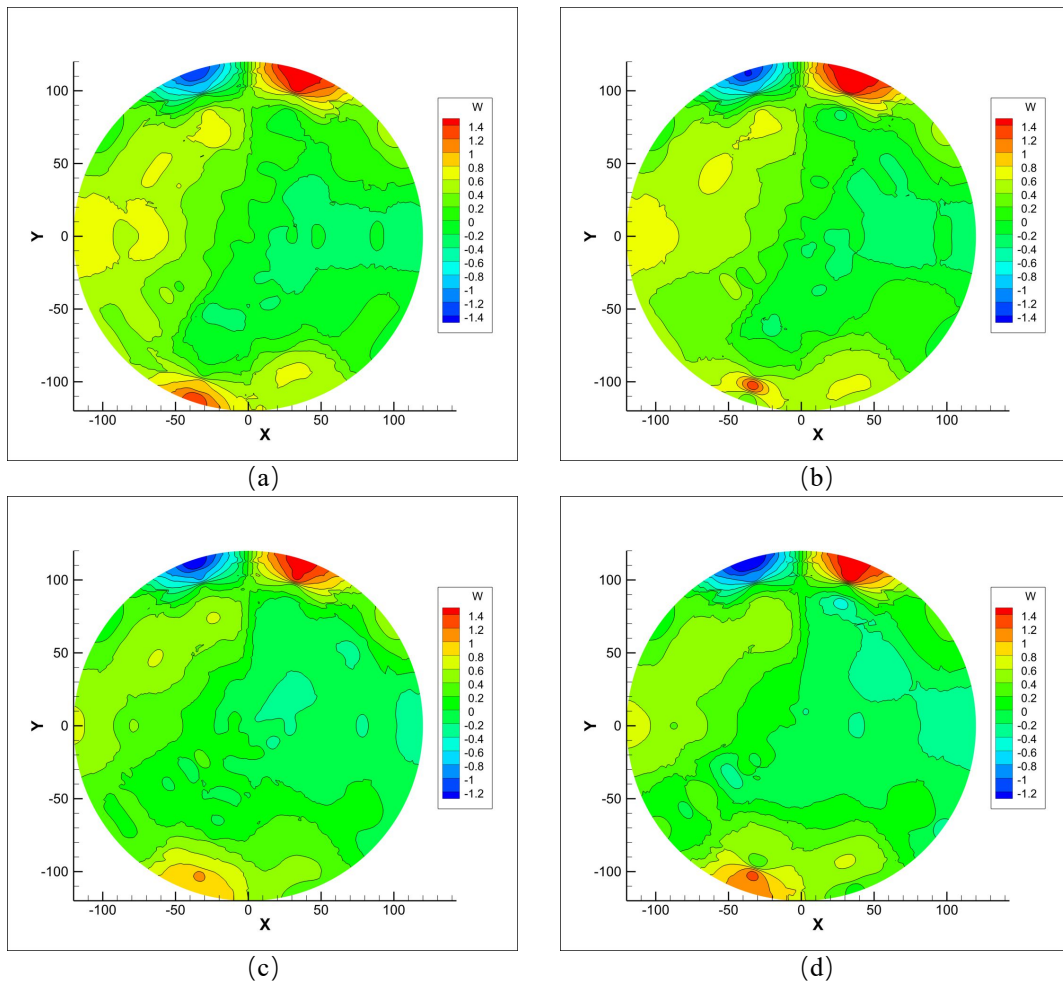
Fig.15. The distribution of velocity components in the X direction on the AIP interface (W)
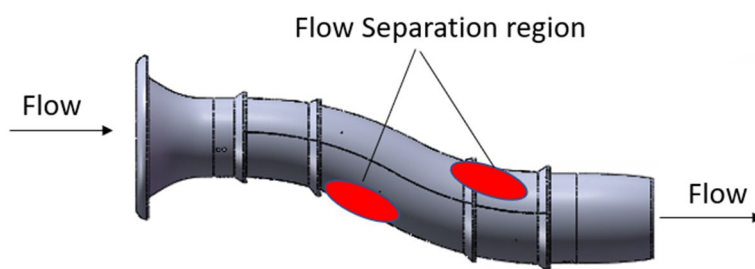
Fig.16. The flow separation region schematic

	U(m/s)	V(m/s)	W(m/s)
(a)	11.99	-0.38	0.13
(b)	11.96	-0.38	0.15
(c)	11.68	-0.49	0.10
(d)	11.98	-0.46	0.09

Table 1. UVW velocity average on the AIP interface

3.2 Vortex generators

Configuration①, as vortex generators, is tested by five excitation modes in this experiment, DC represents duty cycle, M represents modulation frequency, and the detailed information is in the experiment setup. When the modulation frequency is 400, 4 unsteady excitation modes with duty cycles of 10, 20, 30 and 40 are tested, respectively. Three sets of tests were performed with duty cycles of 10 and 20. Only one set of comparative experiments was carried out for the case of duty cycles of 30 and 40. 4 different duty cycles all resulted in a reduction in the stagnation pressure average (as shown in Fig. 17) when plasma was activated, which means total pressure recovery decrease. Additionally, referring to the formation mechanism of starting vortex [1], the duty cycle was set to 50, modulation frequency was set to 1, and a set of tests was carried out. Fig. 17 shows that the last setup (DC50_M1) resulted in a sharp drop in the stagnation pressure average.
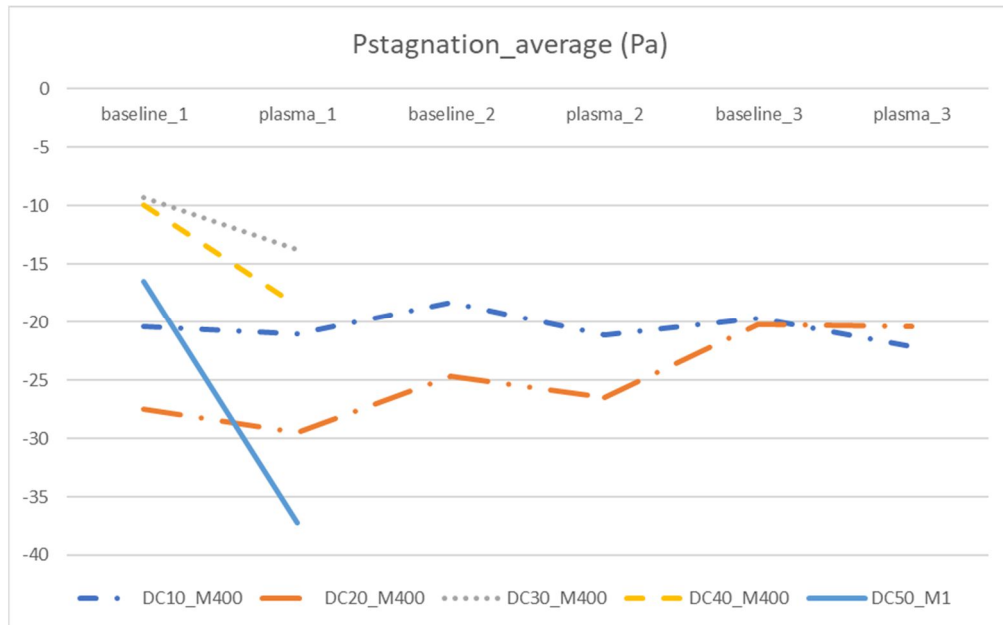
Fig. 17 The average value of the stagnation pressures on the AIP interface (Configuration①:VGs)

When the modulation frequency is 400, the compelling starting vortex may not be formed due to the short time of each plasma excitation period. With the increase of the duty cycle, the jet effect exhibited by the plasma is more pronounced. The direction of the plasma jet is perpendicular to the flow direction of the boundary layer, thus consuming the momentum in the boundary layer to a certain extent. When the modulation frequency is one and DC is 50, according to Whalley *et al.* [1], a starting vortex must be generated in a quasi-static environment. However, the central flow velocity where starting vortex is generated is close to 20m/s, and the generated starting vortex may not have enough strength to resist this speed. The fragmentation of the vortex will cause additional energy loss. Even if the vortex is not broken, under the air velocity of 20m/s, the physical characteristics and motion law of the generated starting vortex still need to be studied, especially for S-duct, which has complex geometric surfaces.

From the results (in Fig. 17), the starting vortex generated in the excitation mode of DC50_M1 is very likely not strong enough to resist the air velocity of nearly 20m/s. There is a problem with using the plasma actuators as vortex generators; the generated vortex is not continuous enough. In a quasi-static environment, DC50_M1, this mode can produce at least a vortex per second (without considering secondary vorticity), and the maximum diameter of the vortex is about 7-8mm [1]. In the case of the air velocity of 20m/s, the vortex is almost pulled into a straight line in the axial direction. To some extent, the body force generated by the plasma actuators is a disturbance to the main flow at this time, and it will consume the momentum inside the boundary layer.

3.3 Wall jet

In this experiment, all the wall jet schemes adopted the excitation mode of 17kv and 4kHz, and the voltage waveform was the square wave. In Fig. 18, (a) is configuration② (3 plasma actuators in parallel), and (b) is configuration③ (5 plasma actuators in parallel). Because of viscous loss, all stagnation pressure average value is negative. As Fig. 18 shows, when the plasma actuators were activated, the stagnation pressure average increased, which means an increase in total pressure recovery. In group(a), three sets of comparative experiments show the

pressure loss decreased by 3%, 47% and 3.9%, respectively. In group(b), the pressure loss in two sets of comparative experiments decreased by 3.17% and 1.47%, respectively. The ambient pressure of group (a) is 97457Pa, and the ambient pressure of group (b) is 98065Pa. The corresponding total pressure recovery is shown in Table 2. Configuration③ has two more plasma actuators than configuration②. In theory, it will provide more momentum to the boundary layer. However, in the experiment, the improvement of total pressure recovery with five plasma actuators does not appear to be better than that of 3 plasma actuators, which may be because although plasma actuators are thin, they provide an additional drag on their own. The two extra plasma actuators downstream may already be in the flow separation region.

(a)   (b)
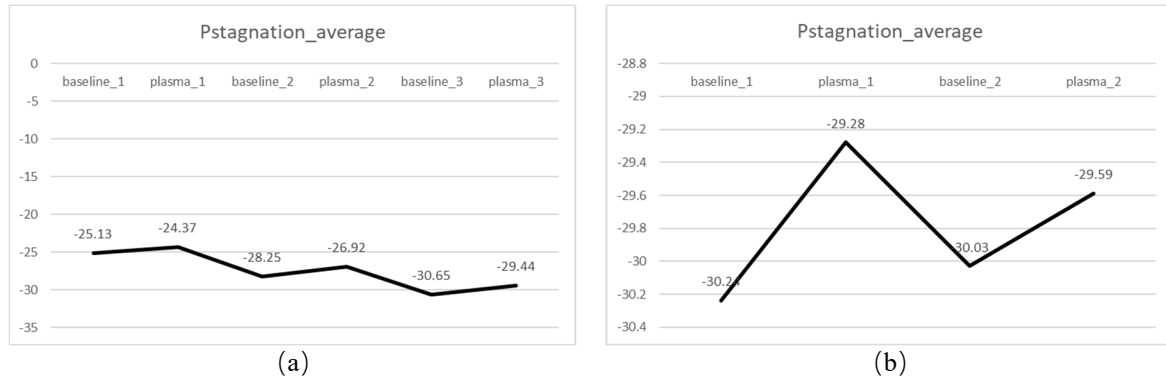
Fig. 18 The average value of the stagnation pressures on the AIP interface

	$f_{baseline}(\%)$	$f_{plasma}(\%)$	$Improvement(\%)$
(a)	99.9742	99.9749	0.0007
	99.9710	99.9724	0.0014
	99.9686	99.9698	0.0012
(b)	99.9692	99.9701	0.0009
	99.9694	99.9698	0.0004

Table 2. The comparison of stagnation pressure recovery

4. Conclusion

Using the plasma actuators as vortex generators, none of the five excitation modes tested showed better performance. When the modulation frequency is 400, with the increase of the plasma excitation time, the total pressure recovery trends are worse because longer excitations mean more pronounced jet effects, and a single excitation cycle may not be enough to generate a starting vortex. When the modulation frequency is set to 1 to ensure that the starting vortex can be generated, because the vortex is not continuous enough and may not have enough strength to resist the airflow of 20m/s, it does not bring better total pressure recovery.

Both configurations have slightly improved total pressure recovery by using the plasma actuators as wall jets. Due to the drag brought by the plasma actuators and two additional plasma actuators in the flow separation region, the 5-plasma actuator array did not perform better than the 3-plasma actuator array.

In conclusion, the plasma-generated starting vortex formation mechanism remains to be further studied. Although the magnitude of the plasma-induced velocity is still tiny, it can still play a role in improving flow separation in high Reynolds number scenarios. To some extent, for the S-duct to improve flow separation, the reliability of plasma actuators as wall jets will be higher.

References

[1] Whalley, R. D., & Choi, K. S. (2012). The starting vortex in quiescent air induced by dielectric-barrier-discharge plasma. *Journal of Fluid Mechanics*, *703*, 192-203.

[2] Jukes, T. N., Segawa, T., & Furutani, H. (2013). Flow control on a NACA 4418 using dielectric-barrier-discharge vortex generators. *AIAA journal*, *51*(2), 452-464.

[3] Jukes, T. N., & Choi, K. S. (2012). Dielectric-barrier-discharge vortex generators: characterisation and optimisation for flow separation control. *Experiments in fluids*, *52*(2), 329-345.

[4] Post, M. L. (2004). *Plasma actuators for separation control on stationary and oscillating airfoils*. University of Notre Dame.

[5] WELLBORN, S., REICHERT, B., & OKIISHI, T. (1992, July). An experimental investigation of the flow in a diffusing S-duct. In *28th joint propulsion conference and exhibit* (p. 3622).

[6] Everett, K., & Durston, D. (1982, January). Theory and calibration of non-nulling seven-hole cone probes for usein complex flow measurement. In *20th Aerospace Sciences Meeting* (p. 232).

[7] J. Brutscher, Datasheet Minipuls 4, 2013

[8] Cattafesta III, L. N., & Sheplak, M. (2011). Actuators for active flow control. *Annual Review of Fluid Mechanics*, *43*, 247-272.

[9] Huang, X., & Zhang, X. (2008). Streamwise and spanwise plasma actuators for flow-induced cavity noise control. *Physics of Fluids*, *20*(3), 037101.

[10] Wojewodka, M. M., White, C., Shahpar, S., & Kontis, K. (2018). A review of flow control techniques and optimisation in s-shaped ducts. *International Journal of Heat and Fluid Flow*, *74*, 223-235.

[11] Gil-Prieto, D., Zachos, P. K., MacManus, D. G., & McLelland, G. (2019). Unsteady characteristics of S-duct intake flow distortion. *Aerospace Science and Technology*, *84*, 938-952.

[12] Wang, J. J., Choi, K. S., Feng, L. H., Jukes, T. N., & Whalley, R. D. (2013). Recent developments in DBD plasma flow control. *Progress in Aerospace Sciences*, *62*, 52-78.

[13] Zhang, W. L., Knight, D. D., & Smith, D. (2000). Automated design of a three-dimensional subsonic diffuser. *Journal of Propulsion and Power*, *16*(6), 1132-1140.

[14] Lefantzi, S., & Knight, D. D. (2002). Automated design optimization of a three-dimensional S-shaped subsonic diffuser. *Journal of propulsion and power*, *18*(4), 913-921.

[15] Aranake, A., Lee, J. G., Knight, D., Cummings, R. M., Cox, J., Paul, M., & Byerley, A. R. (2011). Automated design optimization of a three-dimensional subsonic diffuser. *Journal of Propulsion and Power*, *27*(4), 838-846.

[16] Ghate, D., Isaacs, A., Sudhakar, K., Mujumdar, P., & Marathe, A. (2004, August). 3d-duct design using variable fidelity method. In *10th AIAA/ISSMO Multidisciplinary Analysis and Optimization Conference* (p. 4427).

[17] Khoja, A. H., Tahir, M., & Amin, N. A. S. (2019). Recent developments in non-thermal catalytic DBD plasma reactor for dry reforming of methane. *Energy conversion and management*, *183*, 529-560.